Materials and Design 85 (2015) 221–229

Contents lists available at ScienceDirect

Materials and Design

journal homepage: www.elsevier.com/locate/jmad

Microstructure and mechanical behavior in dissimilar 13Cr/2205 stainless steel welded pipes

K. Bettahar [a,b], M. Bouabdallah [b], R. Badji [a,*], M. Gaceb [c], C. Kahloun [d], B. Bacroix [d]

[a] Welding and NDT Research Centre (CSC), B.P. 64, Cheraga, Algeria
[b] LGSDS, École Nationale Polytechnique, 10, Avenue Hassan Badi, B.P. 182, El Harrach, Algeria
[c] LFEPM, Faculté des hydrocarbures et de la chimie (UMBB), Algeria
[d] LSPM, CNRS, Université Paris 13, 93430 Villetaneuse, France

ARTICLE INFO

Article history:
Received 29 April 2015
Received in revised form 14 June 2015
Accepted 3 July 2015
Available online 6 July 2015

Keywords:
Dissimilar welding
Microstructure
Tensile testing
High cycle fatigue

ABSTRACT

This work aims to investigate the microstructure and the mechanical behavior of dissimilar 13Cr Supermartensitic/2205 Duplex stainless steel welded pipes. A wide variety of microstructures resulting from both solidification and solid state transformation is induced by the fusion welding process across the weld joint. The tensile tests show that the deformation process of the dissimilar weld joint is mainly controlled by the two base materials: the duplex steel at the beginning of the deformation and the supermartensitic one at its end. This is confirmed by the micro-tensile tests showing the overmatching effect of the weld metal. The fatigue tests conducted on dissimilar welded specimens led us to conclude that the weld metal is considered as a weak link of the weld joint in the high cycle fatigue regime. This is supported by its lower fatigue limit compared to the two base materials that exhibit a similar fatigue behavior.

1. Introduction

In the last decades, welding has continuously been an important field of interest since it is the most widely used process in assembling structural components. With the development of more and more innovative materials in several industrial domains, it is necessary to adapt material properties with service conditions. This leads in some cases to join materials having different alloy systems. In this context, dissimilar welding is a promising solution. The necessity of joining different grades of materials takes place in several fields nowadays such as oil and gas, petrochemistry, power plant and automobile industries among others [1–5]. However, the main disadvantage of dissimilar welding is the microstructural heterogeneity generated by the weld thermal cycles that can influence significantly the global and local mechanical behavior of the weld joint. Under optimal operating conditions, the welded components should transfer load on both sides of the structure without being gradually or unexpectedly damaged. Since the mechanical properties are directly related to the microstructure (mismatch effect), the presence of any microstructural heterogeneity causes local heterogeneity of the mechanical behavior of the weld joint. In practice, dissimilar welding of materials, such as 2205 Duplex stainless steel (DSS) and 13% Cr Supermartensitic stainless steel (SMSS), is widely used in gas transportation. DSS and SMSS have both high mechanical properties combined with an excellent corrosion resistance and good weldability despite their microstructures that are different from both morphology and phase constituent aspects. DSSs are known as austenitic–ferritic steels composed of two different phases ferrite and austenite with nearly equal proportions of each [6,7]. The SMSS microstructures consist mainly of martensite with a small amount of retained austenite. Ferrite phase is also frequently found in supermartensitic microstructures and can affect their mechanical behavior if it exceeds a certain proportion [8,9]. In piping industry, some DSS and SMSS components have particular geometries such as flanges, elbows and branch tees. When these regions contain dissimilar weld joints, the risk of crack initiation can be expected due to local microstructural heterogeneity. This difference in microstructure can cause the crack initiation near the fusion line, which is a factor that can increase the local stress concentration in the adjacent heat affected zone as reported in previous works [10]. These cracks can grow under given service conditions causing the fracture of the welded structure [11,12].

Recently, great efforts have been devoted to study the DSS and the SMSS weld joints separately. For the DSS welds, several research works have been carried out to examine the effect of weld metal chemistry and heat input [6], the corrosion behavior in aggressive environments [13], and the effect of post-weld heat treatments on their microstructure and mechanical behavior [14,15]. The strain heterogeneity that occurs during loading and the contribution of austenite and ferrite phases to the global mechanical behavior of the DSS weld joints in either static or dynamic loadings have been well discussed in the literature [16–19].

* Corresponding author.
E-mail address: riadbadji@gmail.com (R. Badji).

http://dx.doi.org/10.1016/j.matdes.2015.07.017
0264-1275/

Table 1
Chemical composition of the DSS, SMSS and the filler metal.

Elements	Cr	Ni	C	Mn	P	S	Cu	Mo	N	Si	Ti	Nb	Al	W
DSS	22.4	5.9	0.021	0.48	0.022	0.0007	0.61	3.65	0.25	0.49	–	–	–	0.64
SMSS	13	7	0.015	1	0.02	0.005	0.25	2.5	0.01	0.05	0.15	0.05	0.055	–
Filler metal	25.1	6.7	0.02	–	–	–	0.5	3.5	0.3	0.4	–	–	–	2

Other microstructural evolutions resulting from the solid state transformation in DSS welds such as austenite reformation in the heat affected zone and precipitation phenomena have been well examined by several authors [20–22]. For the SMSS as well, extensive investigations have been conducted to examine the phase transformations that occur during welding and post-weld heat treatment [9,23,24]. Experimental approaches have also been developed to study the welding residual stresses, the mechanical behavior and the hydrogen stress cracking in SMSS weld joints [25–27]. In spite of the numerous research works that were carried out on the microstructure and the mechanical behavior of DSS and SMSS weld joints, information concerning the deformation behavior of dissimilar weld joints made of these materials needs to be more detailed. Therefore, this work focuses on the microstructural heterogeneity and its impact on the mechanical behavior across the SMSS/DSS weld joint. Due to the complex microstructural heterogeneity, several mechanical tests conducted on specimen having particular geometries are carried out in order to examine precisely the mechanical behavior of each zone separately (base material (BM), heat affected zone (HAZ) and the weld metal (WM)). Specimens containing the complete weld joint have also been prepared in order to examine its global mechanical behavior. The results are discussed in both static and cyclic loadings and related to the microstructure of the weld joint.

2. Material and experimental methods

The materials considered in this work are 13% Cr SMSS and 2205 DSS in the form of tubes of 170 mm outer diameter and 11 mm thickness. Multipass weld joints are elaborated using TIG welding process with ER 2507 Superduplex stainless steel (SDSS) filler material. The chemical compositions of the base and the filler materials are given in Table 1. Sections transverse to the welding direction are prepared for optical metallography and etched using Glyceregia and Beraha's reagents. Microstructural examination of the weld joint is done using a Nikon optical microscope that is also used to estimate the ferrite volume fraction after electrolytic etching by KOH solution. X-ray diffraction (XRD) and energy dispersive spectrometry (EDS) are performed to identify the different phases present in the weld joint. Microhardness profile measurements (HV1) across the weld joint are done according to three profiles P1, P2 and P3 as illustrated in Fig. 1. For the mechanical testing, specimens having different geometries are machined from the welded tube as illustrated in Fig. 2. The global tensile behavior of the weld joint is examined through subsize specimens (see Fig. 3a) that are machined according to ASTM E8 standard [28]. Yield strength (YS), ultimate tensile strength (UTS) and elongation (A %) of the two base materials and the weld metal are determined from the micro-tensile specimens (see Fig. 3b). All the tensile tests are performed at ambient temperature with a strain rate of $0.5 \times 10^{-3}\ s^{-1}$. Charpy V-notch (CVN) subsize specimens are machined according to ASTM A370 standard [29]. The subsize dimension allows the notch to be positioned entirely at the considered zone (BM, HAZ, and WM). Fatigue tests are carried out using universal rotating bending machine. For this purpose, two types of specimens are prepared from the welded pipes: conical and cylindrical ones. The conical specimens are machined according to two configurations by alternating the two base materials with respect to the fixing side (see Fig. 4). These specimens are used to localize the weakest region of the weld joint. The conical part promotes a uniform stress distribution when subjected to a nominal stress given by:

$$\sigma_{nom} = 32 \times M/\pi d^3 \quad (1)$$

where M is the bending moment and d is the specimen diameter at a given position [30]. The fixing method of the fatigue specimens and loadings are illustrated in Fig. 5. The cylindrical shape allows the exposure of a given region to the maximum bending moment at the shoulder. The fatigue tests are done under different levels of constant amplitude loading with a stress ratio $R = -1$ (R is the ratio of the maximal stress to the minimal one) and a rotating frequency $f = 50$ Hz. The fatigue performances of the different regions of the weld joint have been assessed according to Eurocode3 [31], where $N = 5 \times 10^6$ cycles is considered as an indication of fatigue limit and it is assumed that no fatigue failure occurs below this value.

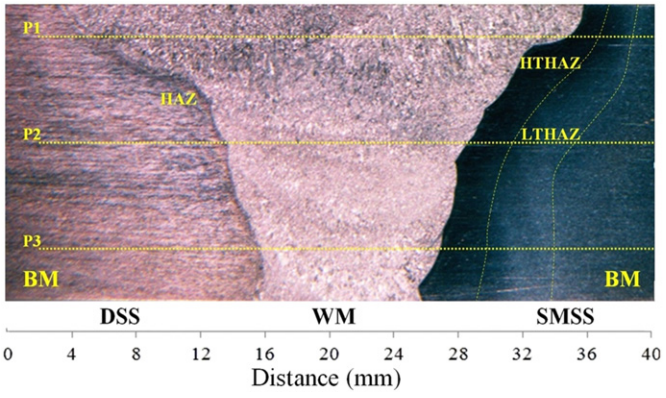

Fig. 1. Optical macrograph of the dissimilar weld joint. P1, P2 and P3 illustrate the microhardness profiles.

3. Results and discussions

3.1. Microstructural evolution across the weld joint

Fig. 1 is an optical macrograph that leads to distinguish easily the different regions of the dissimilar weld joint. The extent of the two HAZs is clearly observed on both sides of the weld joint. Fig. 6a–b shows optical micrographs of the DSS and the SMSS base materials at the as received state. The DSS (Fig. 6a) has a typical banded microstructure constituted of austenite γ (clear) and δ ferrite (dark) with approximately equal amounts. The microstructure of the SMSS (Fig. 6b) is composed mainly of a martensitic matrix, residual austenite and traces of ferrite. It has been reported [32] that martensite is formed from austenite through a displacive mechanism and is arranged in three hierarchical levels: laths, blocks and packets. A given number of packets are delimited by prior austenite grain boundaries as illustrated in Fig. 6b. Table 2 shows the results of the local chemical composition analysis conducted in the different regions of the weld joint using EDS technique. Austenite in the DSS and in the WM is enriched in gamagenic elements whereas ferrite is enriched in alphagenic elements. Retained austenite in the SMSS could not be analyzed by EDS due to its dispersion between the martensitic laths. However, its (111) and (200) peaks have been detected by X-ray diffraction as shown in Fig. 6c. The volume fraction of retained austenite in SMSS can, in some cases, reach 20% as reported in other research works [9,24]. The microstructure of the weld metal (Fig. 7)

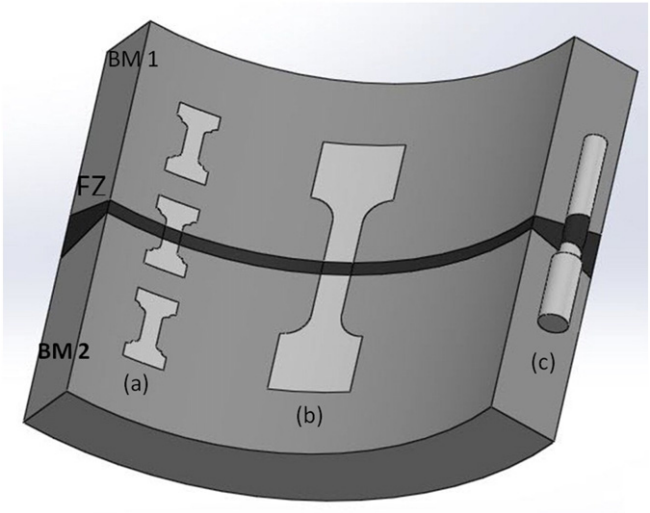

Fig. 2. Schematic illustration of the specimens machined from the welded tube: (a) microtensile specimen, (b) subsize specimen, and (c) fatigue test specimen.

consists of plates and allotriomorph Widmanstätten austenitic grains dispersed within a ferritic matrix. The SDSS is suitable for joining DSS with SMSS materials since it is solidified in a ferritic mode where the crystal structure is the same as that of the SMSS. The epitaxial growth during solidification of the WM is thus favored [11,33]. The optical micrographs presented in Fig. 8a–f illustrate the microstructural evolution that occurs in the HAZ of the SMSS. The different microstructures obtained in this region depend on the maximum peak temperature and can be classified in two categories (see Fig. 8a):

- Those obtained at high temperature constitute the high temperature heat affected zone (HTHAZ).
- Those obtained at low temperature constitute the low temperature heat affected zone (LTHAZ).

(i) The HTHAZ is composed of two subzones: the subzone 1 (that is close to the fusion line) is characterized by a significant growth of the martensitic laths (Fig. 8b) and is called coarse grained HAZ (CGHAZ). In this region the martensitic grain growth is related to the growth of prior austenite grains during the heating thermal cycle. At room temperature, the microstructure of this subzone consists of large untempered martensite delimited by prior austenite grain boundaries. Traces of retained austenite may also exist in this region as reported by Wooling et al. [9]. The subzone 2, also called dual phase zone, is characterized by the presence of ferrite at the prior austenite grain boundaries (Fig. 8c). The volume fraction of ferrite estimated using quantitative metallography technique is about 8%. Table 2, that gives the results of EDS analysis conducted in the different phases present in this region, shows an enhancement of alphagenic elements within the ferrite phase. The presence of ferrite is considered as an indication about the austenite formation mechanism that is mainly controlled by the diffusion of substitutional elements [9]. During cooling, a residual amount of ferrite is trapped at the austenite grain boundaries and within its grains in the form of filaments. These filaments are retained between the martensitic laths after austenite to martensite transformation. This subzone may also contain retained austenite in the form of fine particles dispersed between martensite laths. As the presence of ferrite tends to reduce the toughness of the SMSS, high amounts of gammagenic elements, such as nickel and manganese, are introduced to promote the stability of the austenite and minimize the amount of ferrite. Carrouge et al. [24] reported the existence of another subzone located at the fusion line which is the region that has been partially melted during welding. This region has a martensitic structure that is not detectable by optical microscopy because of its fineness.

(ii) The LTHAZ microstructure results from the transformation that occurs during cooling in the completely or partially austenized regions. As shown in Fig. 8d that corresponds to subzone 3, a considerable grain refinement and a loss of prior austenite grain boundaries characterize this region. This subzone contains an untempered martensite with a possible existence of a stable retained austenite at ambient temperature. The subzone 4 (Fig. 8e) is composed of a mixture of retained austenite and tempered and untempered martensite which has undergone a second quenching and that appears in a dark color in Fig. 8f.

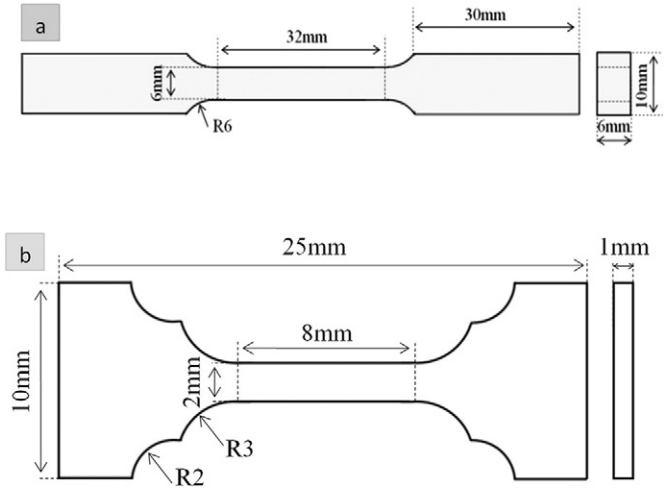

Fig. 3. Schematic illustration of the tensile test specimens: (a) subsize specimen and (b) microtensile specimen.

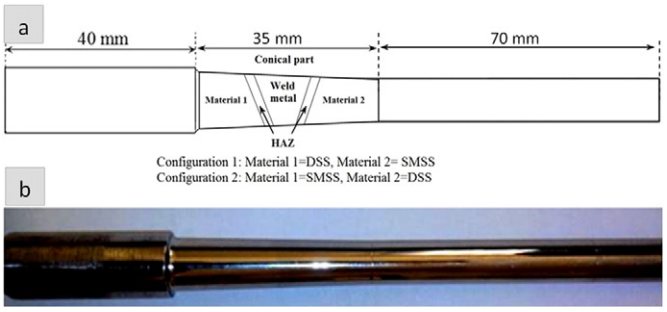

Fig. 4. Schematic illustration of (a) a conical fatigue specimen and (b) actual machined specimen.

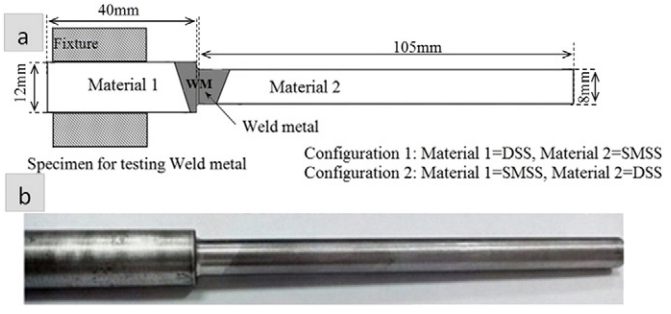

Fig. 5. Schematic illustration of (a) a cylindrical fatigue specimen and (b) actual machined specimen.

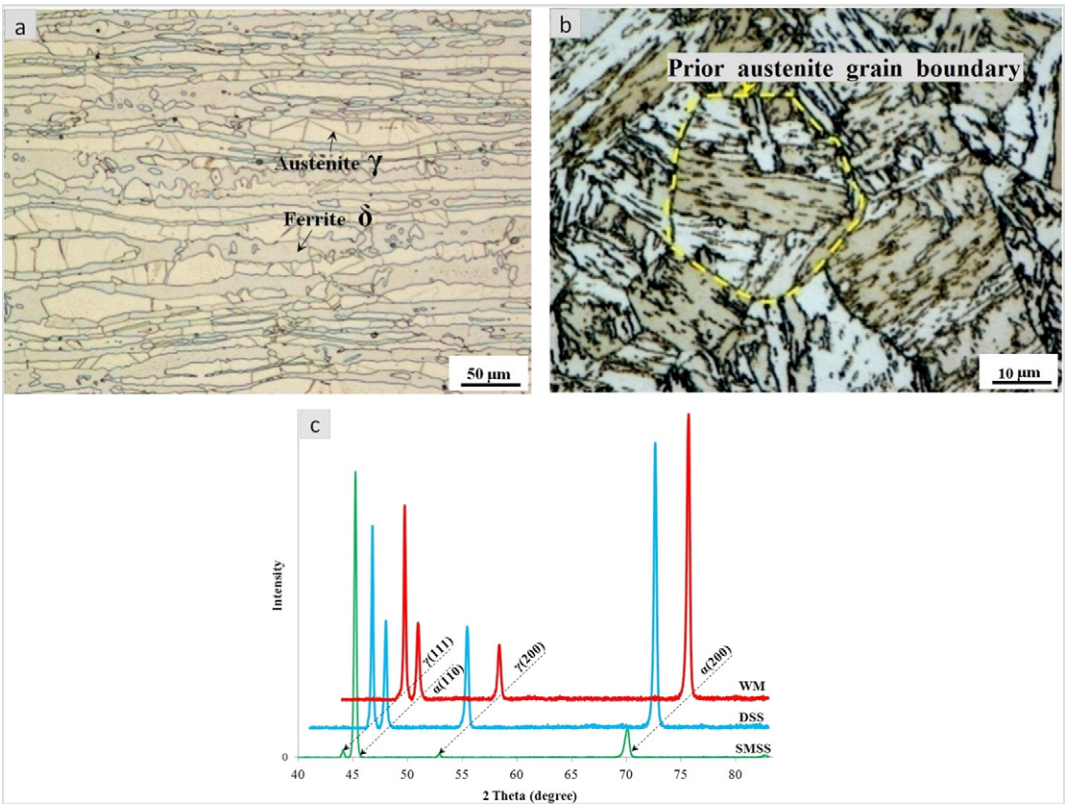

Fig. 6. Optical micrographs of the DSS and the SMSS base materials (a and b), (c) X-ray diffractograms showing the presence of retained austenite in the SMSS.

Some ferrite clusters surrounded by fine martensitic grains are observed in the microstructure of this zone. The presence of the ferrite in this region can be explained by the high molybdenum percentage (a good ferrite stabilizer) which is added generally to promote the resistance against localized corrosion. The complete dissolution of the ferrite phase and its absence during subsequent cooling is not constantly assured.

The SMSS-HAZ subzones (particularly the tempered region) may in some cases contain carbides, carbonitrides and nitrides as reported in other research works [8,9]. Fig. 9 is an optical micrograph that illustrates clearly the effect of the weld thermal cycles on the microstructural evolution in the DSS-HAZ. This zone, depending on the peak temperature achieved, contains two main parts that are the overheated zone (close to the fusion line) and the partially annealed zone. During heating, the microstructure of the overheated zone is fully ferritized due to the high temperature achieved by the weld thermal cycle. During cooling, the austenite is formed through a solid state transformation process and precipitates preferentially at the ferrite/ferrite boundaries and within the ferrite grains. The ferrite/austenite ratio in this region depends on the alloy chemical composition and the cooling rate. Despite the heating effect of the thermal cycles, the partially annealed zone keeps the microstructure banded type that exists in the base material.

3.2. Mechanical behavior

The microhardness evolution across the weld joint is presented in Fig. 10. Apart from the peak recorded in the subzone 3 of the SMSS-LTHAZ (with a maximal value of 325 HV), no significant variation in microhardness is observed in the rest of the weld joint. The high hardness of the subzone 3 can be attributed to the presence of fine untempered martensite. It has been reported [9] that the enrichment of the martensitic matrix in carbon and nitrogen contents may also contribute to the hardness enhancement in this region. A little decrease in hardness is recorded at both sides of this subzone. This drop in hardness is related, on the one hand, to the presence of the ferrite phase and grain coarsening

Table 2
Local chemical compositions obtained by EDS analysis.

Element	DSS material		DSS-HAZ		Weld metal		SMSS-HTHAZ		SMSS
	Austenite	Ferrite	Austenite	Ferrite	Austenite	Ferrite	Martensite	Ferrite	Martensite
Fe	64.39	61.4	63.05	63.06	59.12	56.56	78.96	61.4	78.56
Ni	6.28	3.67	5.67	4.99	8.06	5.17	4.245	3.67	4.4
Cr	22.44	24.92	23.14	23.55	24.67	26.75	14.85	24.92	13.75
Mo	5.38	8.67	6.59	6.98	5.62	8.24	1.685	8.67	1.95
W	0	0	0.00	0.00	2.03	2.86	–		0.70
Mn	1.51	1.33	1.55	1.42	0.5	0.42	0.52	1.33	0.64
Total	100	99.99	100	100	100	100	99.995	99.99	100
Ratio %Cr/%Ni	3.57	6.79	4.08	4.71	3.06	5.17	3.50	6.79	3.125

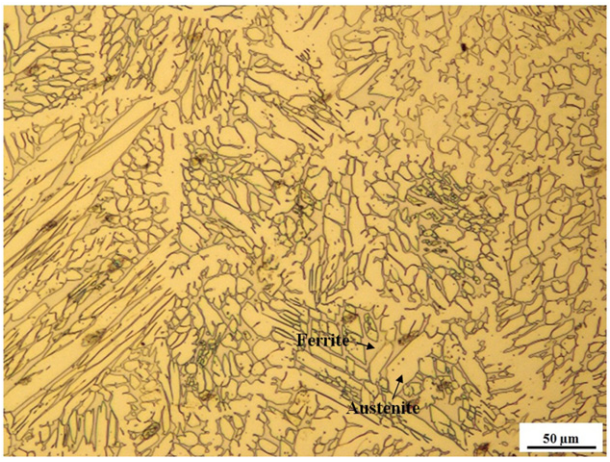

Fig. 7. Optical micrograph of the weld metal.

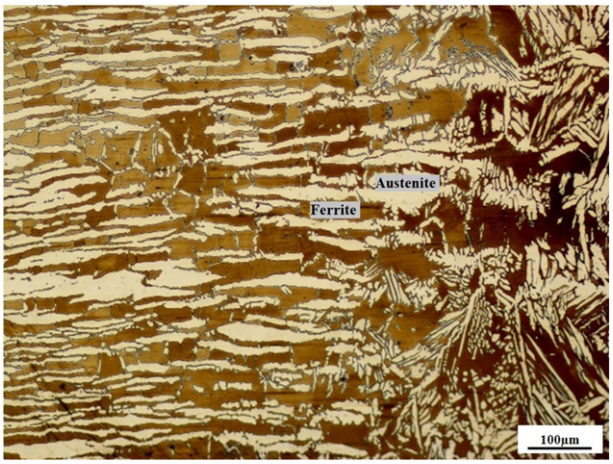

Fig. 9. Optical micrograph of the DSS-HAZ.

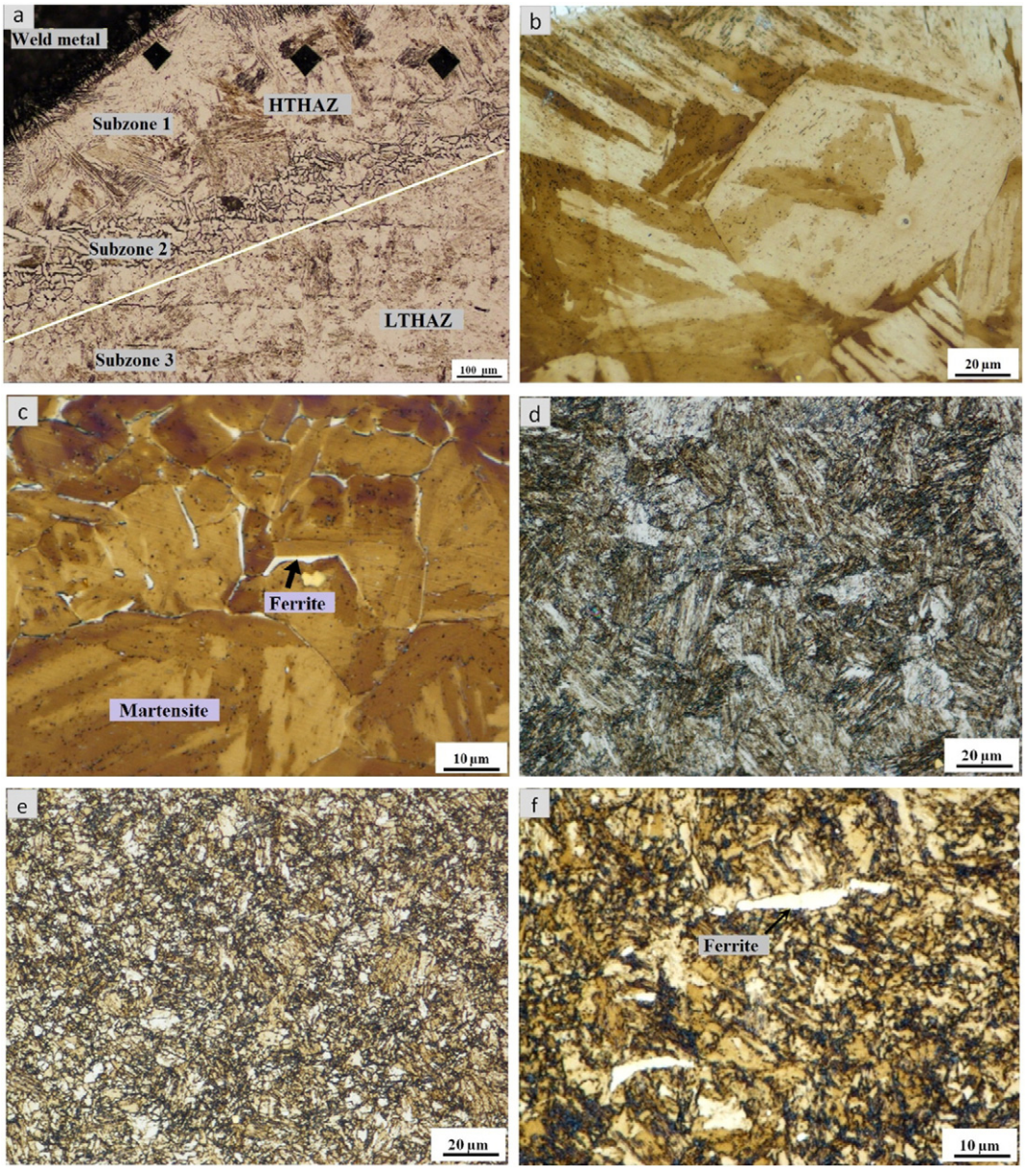

Fig. 8. Optical micrographs of the different subzones of the SMSS-HAZ.

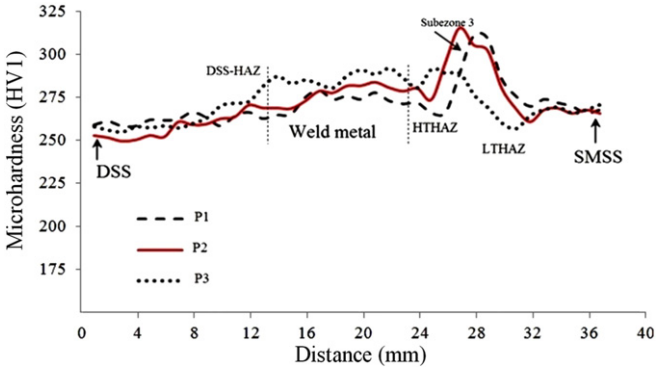

Fig. 10. Microhardness evolution across the weld joint.

for subzones 1 and 2 respectively and, on the other hand, to the additional tempering that happens in subzone 4. The engineering stress strain curve obtained from the subsize tensile specimen containing a dissimilar weld joint is presented in black color in Fig. 11. For all conducted tests, the failure occurred in the SMSS with a non-uniform spreading of plastic deformation through the gage length. The plastic deformation is mainly distributed between the DSS and the SMSS materials. The local tensile behavior of both BMs and the WM obtained from micro-tensile specimens (Fig. 11) shows that the DSS is more susceptible to plastic deformation. The different tensile properties of the base materials, the weld metal and the complete weld joint, are presented in Table 3. Except for the SMSS, the specimen with the complete weld joint presents the less susceptibility to plastic deformation. This can be explained by both the high yield strength (YS) and the ultimate tensile strength (UTS) of the HAZ. However, these two characteristics could not be measured experimentally due to the weak extent of the HAZ that makes the preparation of microtensile specimens difficult. Information concerning the (YS) and the (UTS) of the HAZ, in some cases, can be obtained from hardness measurements. The estimation of tensile properties (yield stress and ultimate tensile stress) from hardness measurements has been extensively reported in the literature [34,35]. Since the hardness level of both HAZs is higher than that of the two BMs, the strengths corresponding to the onset of their plastic deformation may be superior to the ones of the BMs. More detailed investigation of the mechanical heterogeneity across the weld joint can be achieved by introducing a global strength mismatch factor *M*. This factor is defined as the ratio of the yield strength of the WM to that of the BM [36]. Since the weld joint contains two different base materials, the *M* factor can have two values: one is relative to the DSS material $M_{(WM/DSS)} = 1.25$ and the other to the SMSS material $M_{(WM/SMSS)} = 1.07$ (we note

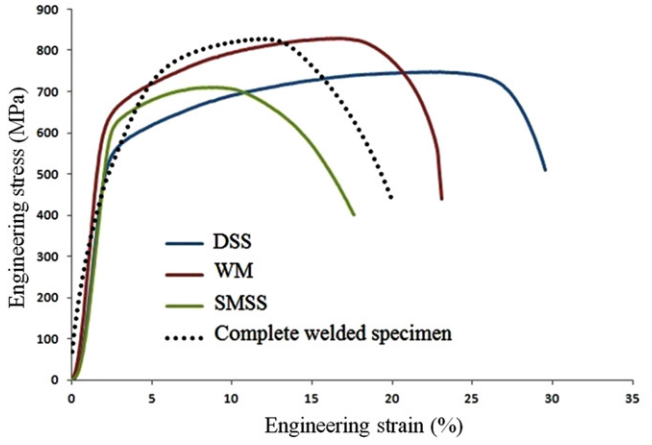

Fig. 11. Engineering stress strain curves obtained from subsize and microtensile specimens.

Table 3
Mechanical properties obtained from the subsize and microtensile specimens.

	DSS	WM	SMSS	Welded specimen
Young's modulus (GPa)	202	231	215	–
Yield strength 0.2% (MPa)	520	650	600	540
Ultimate tensile strength (MPa)	750	820	705	830
Elongation (%)	30	23	17.5	20
Yield ratios	0.69	0.85	0.79	0.65

that $M_{(WM/DSS)} > M_{(WM/SMSS)} > 1$). These calculations lead us to conclude that the superduplex filler metal used for joining 13Cr SMSS to 2205 DSS provides a global overmatching effect. These results are in good agreement with those published in previous works [11]. The local mismatch factor (defined as the ratio of the WM yield strength to that of the HAZ) may also have two values. It is thus expected that the weld joint exhibit a local overmatching effect for the DSS-HAZ and a local undermatching effect for the SMSS-HAZ. To compare the ability of each region of the weld joint to local plastic deformation, the yield ratios of the two BMs and the WM are calculated. The yield ratio (YR) that is considered as a good indicator of a material's ability to plastic deformation is defined as the ratio of its yield strength to its tensile strength. The lower the yield ratio is, the higher the ability of the material to plastic deformation [37]. The different values of the yield ratios obtained are: 0.69, 0.85, and 0.79 corresponding to DSS, SMSS and the WM respectively. We note that the WM is about 75% of ductility of the DSS and 120% of that of the SMSS. For the SMSS, the stress–strain curve attains very quickly the maximum hardening (UTS) value and starts the necking stage before the DSS reaches 30% of its total uniform elongation. The onset of the global yielding of the weld joint in tensile testing is controlled by the DSS whereas its offset (maximum yielding) is controlled by the SMSS. The results of the impact tests presented in Fig. 12 indicate that the WM has the lowest impact energy. The DSS exhibits the highest impact energy that is attributed to the particularity of its dual phase banded microstructure. The impact energy of the SMSS is slightly less than the one of the DSS because of the martensitic structure, but it is still quite high in comparison to those of the WM and the SMSS-HAZ. The presence of retained austenite in the SMSS promotes its toughness as reported by Carrouge et al. [24].

3.3. Fatigue behavior of the weld joint

The experimental results obtained from the fatigue tests conducted in this work are interpreted on the basis of the stress level repartition for both configurations presented in Figs. 4 and 5. Table 4 that gives the results of the experimental fatigue tests conducted on the conical specimens indicates that the fatigue limit of the weld joint is 300 MPa corresponding to 5×10^6 cycles. For all the conducted tests, the failure occurred in the WM (at the middle of the conical part). There is no failure that occurred in the two BMs or in the two HAZs. Fig. 13a shows the experimental S–N curves of both BMs and the WM obtained from the

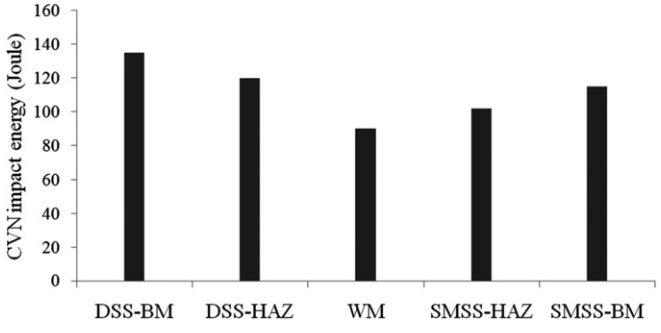

Fig. 12. Evolution of the impact energy across the weld joint.

Table 4
Fatigue test results conducted on conical specimens.

Conical specimens	Calculated stress (MPa)	Cycle number	Observation
Configuration 1	275	$>5\times10^6$	No failure
Configuration 1	290	$>5\times10^6$	No failure
Configuration 1	305	2,442,303	Partial failure occurred in the WM
Configuration 2	280	$>5\times10^6$	No failure
Configuration 2	290	$>5\times10^6$	No failure
Configuration 2	300	3,286,379	Partial failure occurred in the WM

cylindrical specimens. Examples of the failed conical and cylindrical specimens are presented in Fig. 13b. The experimental curves are fitted using a power law in the form of $y = a \cdot x^b$ (where: a and b are the fatigue parameters or Basquin coefficients). Despite some scatter of the results namely for the WM, the shape of the curves shows a decrease in lifetimes with increasing applied stress. For high loads corresponding to life times below 5×10^5 cycles, both BMs and the WM present a quite similar behavior despite their microstructures that are different in morphology, phase constituent and proportion. As the stress level decreases, the fatigue limit of the WM decreases more rapidly than that of the BMs until 6×10^5 cycles (see Fig. 13a). At this stage, the fatigue limits of the two BMs and the WM obtained from the cylindrical specimens are around 300 MPa and 250 MPa respectively. Note that all the cylindrical specimens tested in this work failed at the shoulders where the stress level is maximum. For the conical specimens, all the regions of the weld joint are subjected to the same constant bending moment (M_f) for which a nominal stress can be considered. However, the situation is different for the cylindrical specimens where there is no nominal stress. The difference in fatigue limit obtained from the two geometries can be explained by introducing the concept of the stress concentration factor in static and dynamic loadings. Peterson [38] defined two factors: the elastic stress concentration factor K_t and the fatigue strength reduction factor K_f. K_t is defined as the ratio of the calculated peak stress in the presence of a stress concentrator, to the nominal stress that would be uniformly distributed in the absence of a stress concentrator. This factor is solely related to the geometrical and loading considerations. For the cylindrical specimens, the K_t factor has the same value for the WM and the two BMs which is equal to 1.3 according to Peterson's charts [38]. The K_f factor is defined by the ratio of the fatigue limit of unnotched specimen to the fatigue limit of a notched specimen:

$$K_f = \sigma_{d\ unotched}/\sigma_{d\ notched}. \tag{2}$$

Considering the conical specimens as notch free ones and the cylindrical specimens as notched ones, thus: $K_{f\,experimental\ (WM)} = (300/250) = 1.2$. This factor reflects the level of reduction in fatigue limit due to the stress concentrator and it is not considered as a correction for the actual applied stresses. The K_f factor is situated between 1 and K_t ($1 < K_f < K_t$). The expression that correlates between the two factors (K_t) and (K_f) is given by Eq. (3) with introducing a notch sensitivity factor (q) that varies from 0 to 1 ($K_f = 1$ for insensitive materials to notch effect and $K_f = K_t$ for fully notch sensitive materials).

$$q = (K_f - 1)/(K_t - 1) \tag{3}$$

It has been established [38,39] that the notch sensitivity factor (q) depends on the elastic properties of materials and the notch radius.

$$q = 1/(1 + (a_p/\rho)) \tag{4}$$

a_p is a material constant given by:

$$a_p = 0.0254 \times (2079/\sigma_u)^{1.8} \tag{5}$$

where ρ is the notch radius and σ_u is the ultimate tensile strength.

From Eq. (3):

$$K_f = q \times (K_t - 1) + 1. \tag{6}$$

The K_f values for the two BMs and the WM are calculated using Eqs. (4), (5) and (6). Thus, $K_{f(DSS)} = 1278$, $K_{f\ (SMSS)} = 1275$ and $K_{f\ (WM)} = 1281$.

Consequently the nominal fatigue limits of the DSS and SMSS can be calculated using the experimental results and Eq. 2. Thus:

$$\begin{aligned} &\sigma_{d\ unotched} = K_f \times \sigma_{d\ notched} \\ &\sigma_{d\ unotched(DSS)} = K_{f(DSS)} \times \sigma_{d\ notched(DSS)} = 383.37\ \text{MPa} \\ &\sigma_{d\ unotched(SMSS)} = K_{f(SMSS)} \times \sigma_{d\ notched(SMSS)} = 382.65\ \text{MPa} \\ &\sigma_{d\ unotched(WM)} = K_{f(WM)} \times \sigma_{d\ notched(WM)} = 320.24\ \text{MPa}. \end{aligned} \tag{7}$$

According to the foregoing results, it seems that the two base materials have relatively the same level of the fatigue limit. The WM has the lowest resistance in high cycle fatigue regime compared to the other parts of the weld joint despite its high tensile and hardness characteristics. This can be attributed to the rapid crack propagation that occurs in this region independent of the crack initiation sensitivities. It has been reported [40] that the local impact energy is directly related to the corresponding local toughness which expresses the resistance to rapid crack propagation. Since the WM has the lowest impact energy, its susceptibility to fatigue damage can be expected. The tensile residual stress induced by the welding process can also contribute efficiently to the early crack nucleation in the WM as reported by Akselsen et al. [41]. Fig. 14a–c shows the surface fatigue fractures of the WM, the DSS and the SMSS respectively. It is observed that the two BMs and the WM present a similar failure mechanism when subjected to rotating bending

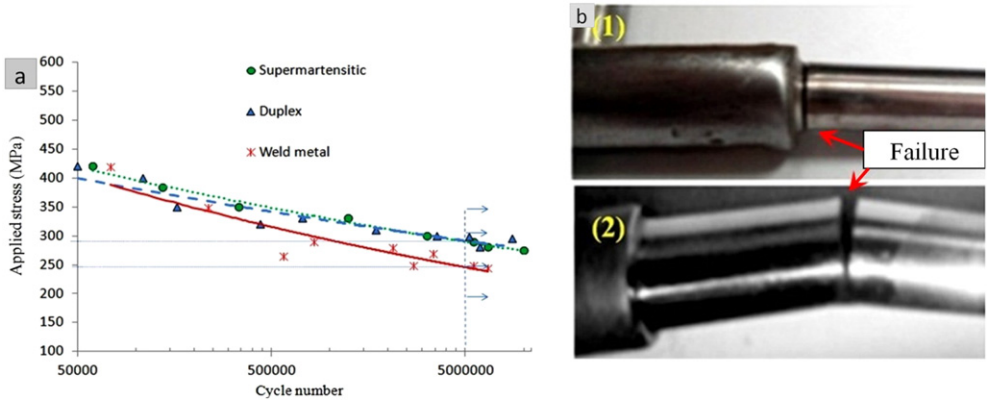

Fig. 13. (a) S–N diagrams of the two base materials and the weld metal. (b) Examples of failed conical and cylindrical specimens.

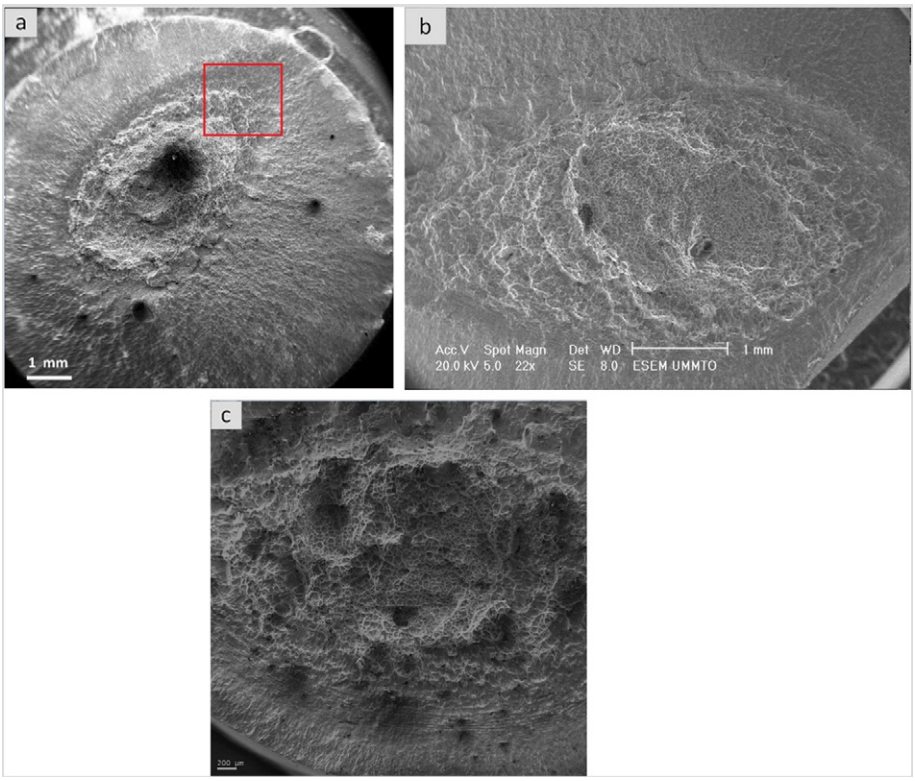

Fig. 14. Scanning electron macrographs of the surface fatigue fractures of (a) the WM, (b) the DSS and (c) the SMSS.

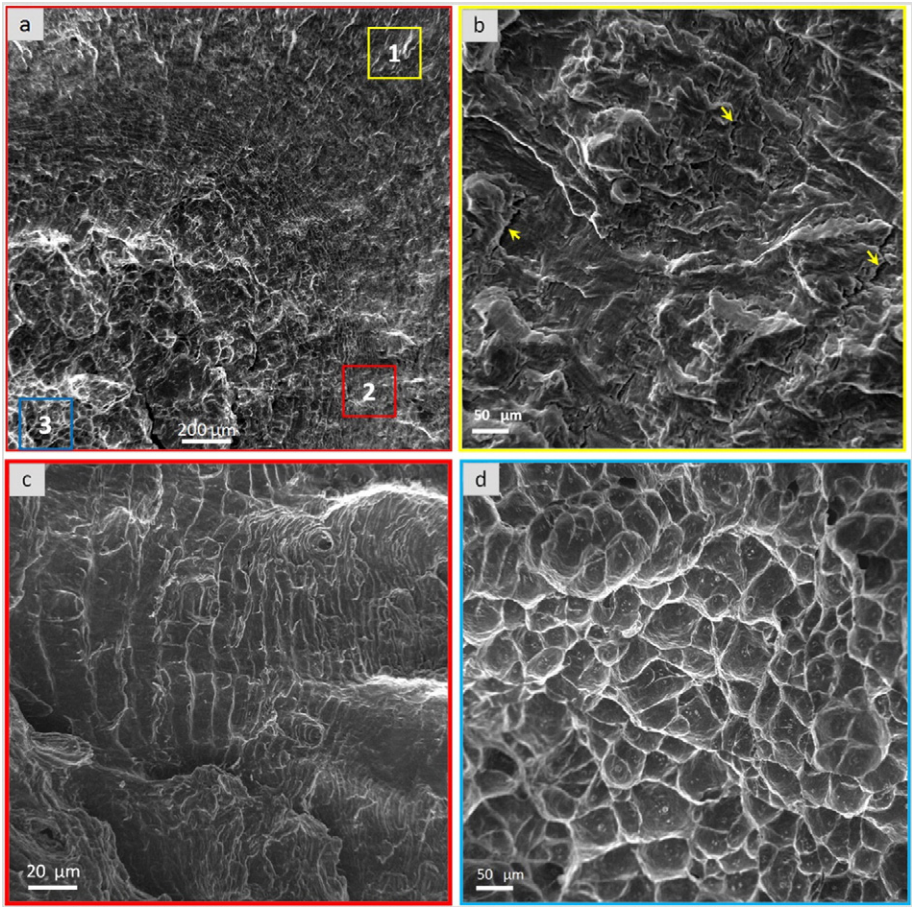

Fig. 15. Fractographs showing the three fatigue fracture modes that occurred in the WM. (a) Magnification of the highlighted section of Fig. 13a, (b) brittle fracture mode, (c) fatigue striations, (d) ductile fracture mode.

fatigue. The fracture seems to initiate in the outer surface where the applied stress is maximal. Fig. 15a that is a magnification of the highlighted section in Fig. 14a, leads us to distinguish the different modes of failure that occur in the WM. These modes are illustrated in Fig. 15b–d obtained from a high magnification of regions (1), (2) and (3) of Fig. 14a and b that illustrates a transgranular brittle fracture display cleavage accompanied by plastic deformation; some micro-cracks are visible and indicated by arrows. Fig. 15c shows fatigue striations that seem to be uniform and mark the crack propagation direction. These striations are concentric and they separate the ductile and brittle failure modes. They may originate from the acceleration and the deceleration of the crack growth process during cyclic loading. Fig. 15d leads us to distinguish easily the dimples and the microporosities that are signs of the plastic deformation. In this location, the applied stress has exceeded the material yield stress. This surface is typical for a ductile fracture.

4. Conclusion

The microstructural evolution and the mechanical behavior of a 13Cr SMSS/2205 DSS weld joint have been studied in both static and cyclic loadings. The main conclusions of this work are summarized as follows:

- Dissimilar welding of 13Cr SMSS and 2205 DSS results in a strong microstructural heterogeneity that concerns microstructure, phase constituent, morphology and phase-volume fractions in the heat affected zones. While two distinguished zones constitute the DSS-HAZ, four subzones are observed in the SMSS-HAZ.
- The tensile tests conducted on subsize specimens containing the complete weld joint and microtensile ones machined from each zone separately led us to conclude that the onset of the global yielding of the dissimilar weld joint is controlled by the DSS whereas its offset (maximum yielding) is controlled by the SMSS.
- While a global overmatching effect provided by the superduplex filler metal is recorded, local overmatching and undermatching effects can be expected for the DSS and SMSS HAZs respectively.
- The high cycle fatigue behavior of the weld joint is mainly controlled by the weld metal. This region is considered as a weak link in terms of fatigue performance due to its lower fatigue limit (300 MPa at 5×10^6 cycles) compared to the two base materials that present a similar fatigue behavior with a fatigue limit of 370 MPa.

References

[1] M. Rossini, P. Russo Spena, L. Cortese, P. Matteis, D. Firrao, Investigation on dissimilar laser welding of advanced high strength steel sheets for the automotive industry, Mater. Sci. Eng. A 628 (2015) 288–296.
[2] J. Cao, et al., Microstructure and mechanical properties of dissimilar materials joints between T92 martensitic and S304H austenitic steels, Mater. Des. 32 (2011) 2763–2770.
[3] G. Chen, et al., Microstructures and mechanical properties of T92/Super 304H dissimilar steel weld joints after high-temperature ageing, Mater. Des. 44 (2013) 469–475.
[4] R. Mittal, B.S. Sidhu, Microstructures and mechanical properties of dissimilar T91/347H steel weldments, J. Mater. Process. Technol. 220 (2015) 76–86.
[5] S. Wang, Q. Ma, Y. Li, Characterization of microstructure, mechanical properties and corrosion resistance of dissimilar welded joint between 2205 duplex stainless steel and 16MnR, Mater. Des. 32 (2011) 831–837.
[6] V. Muthupandi, P. BalaSrinivasan, S.K. Seshadri, S. Sundaresan, Effect of weld metal chemistry and heat input on the structure and properties of duplex stainless steel welds, Mater. Sci. Eng. A358 (2003) 9–16.
[7] R. Badji, B. Bacroix, M. Bouabdallah, Texture, microstructure and anisotropic properties in annealed 2205 duplex stainless steel welds, Mater. Charact. 62 (9) (2011) 833–843.
[8] X.P. Ma, L.J. Wang, C.M. Liu, S.V. Subramanian, Microstructure and properties of 13Cr5Ni1Mo0.025Nb0.09V0.06N supermartensitic stainless steel, Mater. Sci. Eng. A 539 (2012) 271–279.
[9] P. Woollin, D. Carrouge, Heat affected zone microstructures in supermartensitic stainless steels, Conference on Supermartensitic Stainless Steels; 2002 Oct 3–4; Brussels, Belgium, 2002.
[10] T. Moltubakk, C. Thaulow, Z.L. Zhang, Application of local approach to inhomogeneous welds. Influence of crack position and strength mismatch, Eng. Fract. Mech. 62 (1999) 445–462.
[11] A. Carpinteri, C. Ronchei, D. Scorza, S. Vantadori, Fracture mechanics based approach to fatigue analysis of welded joints, Eng. Fail. Anal. 49 (2015) 67–78.
[12] W. Fricke, Fatigue analysis of welded joints: state of development, Mar. Struct. 16 (2003) 85–200.
[13] D.H. Kang, H.W. Lee, Study of the correlation between pitting corrosion and the component ratio of the dual phase in duplex stainless steel welds, Corr. Sci. 74 (2013) 396–407.
[14] R. Cervo, P. Ferro, A. Tiziani, Annealing temperature effects on super duplex stainless steel UNS s32750 welded joints. I: microstructure and partitioning of elements, J. Mater. Sci. 45 (2010) 4369–4377.
[15] R. Badji, M. Bouabdallah, B. Bacroix, C. Kahloun, K. Bettahar, N. Kherrouba, Effect of solution treatment temperature on the precipitation kinetic of σ phase in 2205 duplex stainless steel welds, Mater. Sci. Eng. A 496 (2008) 447–454.
[16] W.Y. Hsiao, S.H. Wang, C.Y. Chen, J.R. Yang, W.S. Lee, Effects of dynamic impact on mechanical properties and microstructure of special stainless steel weldments, Mater. Chem. Phys. 111 (2008) 172–179.
[17] M.C. Young, L.W. Tsay, C.S. Shin, S.L.I. Chan, The effect of short time post-weld heat treatment on the fatigue crack growth of 2205 duplex stainless steel welds, Int. J. Fatigue 29 (2007) 2155–2162.
[18] J. Pilhagen, H. Sieurin, R. Sandström, Fracture toughness of a welded super duplex stainless steel, Mater. Sci. Eng. A 606 (2014) 40–45.
[19] R. Badji, T. Chauveau, B. Bacroix, Texture, misorientation and mechanical anisotropy in a deformed dual phase stainless steel weld joint, Mater. Sci. Eng. A 575 (2013) 94–103.
[20] H. Sieurin, R. Sandstrom, Austenite reformation in the heat-affected zone of duplex stainless steel 2205, Mater. Sci. Eng. A 418 (2006) 250–256.
[21] C.F. Willis, R. Gronsky, T.M. Devine, Carbide precipitation in welds of two-phase austenitic–ferritic stainless steel, Metall. Trans. A 22 (1991) 2889–2902.
[22] Yutaka S. Sato, Hiroyuki Kokawa, Preferential precipitation site of sigma phase in duplex stainless steel weld metal, Scr. Mater. 40 (6) (1999) 659–663.
[23] C. Gesnouin, A. Hazarabedian, P. Bruzzoni, J. Ovejero-Garc, P. Bilmes, C. Llorente, Effect of post-weld heat treatment on the microstructure and hydrogen permeation of 13CrNiMo steels, Corr. Sci. 46 (2004) 1633–1647.
[24] D. Carrouge, H.K.D.H. Bhadeshia, P. Woollin, Effect of δ ferrite on impact properties of supermartensitic stainless steel heat affected zones, Sci. Technol. Weld. Join. 9 (2004) 377–389.
[25] D. Thibault, P. Bocher, M. Thomas, Residual stress and microstructure in welds of 13%Cr–4%Ni martensitic stainless steel, J. Mater. Process. Technol. 209 (2009) 2195–2202.
[26] A. Griffiths, W. Nimmo, B. Roebuck, G. Hinds, A. Turnbull, A novel approach to characterizing the mechanical properties of super 13 Cr steel welds, Mater. Sci. Eng. A 384 (2004) 83–91.
[27] K.G. Solheim, J.K. Solberg, Hydrogen induced stress cracking in supermartensitic stainless steels — stress threshold for coarse grained HAZ, Eng. Fail. Anal. 32 (2013) 348–359.
[28] ASTM E8 M, Standard test methods for tension testing of metallic materials, Metric 01 (01) (2003) 20–23.
[29] ASTM A 370, Standard Test Methods and Definitions for Mechanical Testing of Steel Products, 2003.
[30] A.M. Eleiche, M.M. Megahed, N.M. Abd-Alla, Low-cycle fatigue in rotating cantilever under bending II: experimental investigations on smooth specimens, Int. J. Fatigue 18 (8) (1996) 577–592.
[31] Eurocode 3, Design of steel structures. Part 1.1. General rules and rules for buildings, ENV 1993-1-11992.
[32] S. Morito, Y. Edamatsu, K. Ichinotani, T. Ohba, T. Hayashi, Y. Adachi, T. Furuhara, G. Miyamoto, N. Takayama, Quantitative analysis of three-dimensional morphology of martensite packets and blocks in iron–carbon–manganese steels, J. Alloys Comp. 577S (2013) S587–S592.
[33] K.D. Ramkumar, G. Thiruvengatam, S.P. Sudharsan, D. Mishra, N. Arivazhagan, R. Sridhar, Characterization of weld strength and impact toughness in the multi-pass welding of super-duplex stainless steel UNS 32750, Mater. Des. 60 (2014) 125–135.
[34] M.O. Lai, K.B. Lim, On the prediction of tensile properties from hardness tests, J. Mater. Sci. 26 (1991) 2031–2036.
[35] P. Zhang, S.X. Li, Z.F. Zhang, General relationship between strength and hardness, Mater. Sci. Eng. A 529 (2011) 62–73.
[36] H. Zhou, F. Biglari, C.M. Davies, A. Mehmanparast, K.M. Nikbin, Evaluation of fracture mechanics parameters for a range of weldment geometries with different mismatch ratios, Eng. Fract. Mech. 124–125 (2014) 30–51.
[37] A.C. Bannister, J.R. Ocejo, F. Gutierrez-Solana, Implications of the yield stress/tensile stress ratio to the SINTAP failure assessment diagrams for homogeneous materials, Eng. Fract. Mech. 67 (2000) 547–562.
[38] Walter D. Pilkey, Peterson's Stress Concentration Factors, 2nd ed. Wiley& Sons, New York, 1997.
[39] Yung-Li Lee, Jwo Paw, Richard B. Hathaway, Mark E. Barkey, Fatigue Testing and Analysis (Theory and Practice). Elsevier Butterworth–Heinemann 200 Wheeler Road, Burlington, MA 01803, USA Linacre House, Jordan Hill, Oxford OX2 8DP, UK; 2005
[40] Y. Tanaka, T. Iwadate, K. Suzuki, Small specimen measurements of dynamic fracture toughness of heavy section steels for nuclear reactor pressure vessels, Int. J. Pres. Piping 31 (1988) 221–236.
[41] O.M. Akselsen, R. Aune, V. Olden, G. Rørvik, Effects of phase transformations on residual stresses in welding of stainless steels, Int. J. Offshore Polar Eng. 17 (2) (2007) 145–151.